Calibration of a Rotating 2D Laser Range Finder using Point-Plane Constraints

Edmond Wai Yan So, Filippo Basso, Emanuele Menegatti

Abstract:

A common method used to obtain 3D range data with a 2D laser range finder is to rotate the sensor. To combine the 2D range data obtained at different rotation angles into a common 3D coordinate frame, the axis of rotation relative to the mirror center of the laser range finder should be known. This axis of rotation is a line in 3D space with four degrees of freedom. This paper describes a method for recovering the parameters of this rotational axis, as well as the extrinsic calibration between the rotational axis and a camera. It simply requires scanning several planar checkerboard patterns that are also imaged by a static camera. In particular, we use only correspondences between lines in the laser scans and planes in the camera images, which can be established easily even for non-visible lasers. Furthermore, we show that such line-on-plane correspondences can be modelled as point-plane constraints, a problem studied in the field of robot kinematics. We use a numerical solution developed for such point-plane constraint problems to obtain an initial estimate, which is then refined by a nonlinear minimization that minimizes the „line-of-sight" errors in the laser scans and the reprojection errors in the camera image. To validate our proposed method, we give experimental results using a LMS-100 mounted on a pan-tilt device in a nodding configuration.

Keywords: *laser range finder, extrinsic calibration, point-plane constraints, minimal conditions, maximum likelihood estimate*

1. Introduction

Laser range finders (LRF) are used extensively in mobile robots for many tasks, including localization, mapping, and obstacle avoidance. 2D LRFs, such as the SICK LMS-200 and the Hokuyo UTM-30LX, have proved to be popular due to their low costs, although the range measurement data are confined to a single plane. 3D LRFs such as the Velodyne HDL-64 are commercially available, but they are not as widely employed due to their high costs. Affordable 3D range sensors such as time-of-flight / phase-shift cameras (e.g. Swiss Ranger SR4000) and structured-light cameras (e.g. Microsoft Kinect) have recently became available, but they have limited range and are usually confined to indoor use.

An economical method for obtaining 3D range data from a 2D LRF is to rotate the LRF, by using a stepper motor or a pan-tilt device. To combine the LRF range data obtained at different angles into a single coordinate frame, the axis of rotation relative to the mirror center inside the laser ranger finder is required. As shown in Fig. 2, this rotational axis is a line in 3D space with 4 degrees of freedom.

In this paper, we propose a method to recover the parameters of this axis by scanning several large planar checkerboard patterns with the LRF and imaging the checkerboards with a static camera. In particular, we use only correspondences between lines in the laser scans and planes in the camera images, which can be established easily even for non-visible lasers.

Essentially, the proposed calibration procedure consists of three main steps. First, static camera-LRF calibration is performed at two different rotational angles. Although there already exists numerous solutions to this problem in the literature, we propose instead to model the calibration problem using kinematics point-plane constraints. This allows us to use the minimum number of calibration planes, reducing the amount of time for data acquisition and processing.

In the second step, we obtain an initial estimate for the rotational axis by performing a screw decomposition of the relative LRF motion estimated in the first step.

In the final step, starting with an initial estimate of the parameters of the rotational axis, a nonlinear minimization is performed to recover its precise values. For the cost function, instead of the perpendicular point-to-plane distance that is commonly used, we propose to minimize the ``line-of-sight'' errors, which directly models the noise in the LRF range measurements.

2. Related Work

Several methods have been proposed to calibrate a static 2D LRF with a static camera [1--4]. The most commonly-used solution is the one given by Zhang [1], which uses correspondences between lines in a laser scan and planes in a camera image, as we do in this paper. In [3] and [4], correspondences between a point in the laser scan and a line in a camera image are used. For calibration between a static 3D LRF and a static camera, Unnikrishnan [5] gives a solution similar to Zhang's that uses correspondences between planes in a laser scan and planes in a camera image. As we will explain in §5, all of these methods can be cast as point-plane constraints problems. All of these work aim to find the transformation between the coordinate frames of a LRF and a camera.

On the other hand, our current work is focused on locating the axis of rotation of an articulated 2D LRF. The solution used by one of the earliest system

is to have the supporting bracket precisely machined so that the axis of rotation is aligned with the mirror center of the LRF [6, 7]. If this is not the case, mechanical drawings and hand measurement are used to manually locate the offset distance [8]. For the rotating 2D LRF described in [9], a more elaborate method described by Weingarten [10] is used, which involves scanning a cuboid room measured by hand. In all of these methods, the axis of rotation is assumed to be perfectly aligned with one of the primary axis of the LRF, and only the offset distance is determined. In this paper, by modelling the axis of rotation with 4 degrees of freedom, we allow for rotational misalignment to occur.

In [11], Pradeep et al. describes a general calibration method for sensors on an articulated kinematic chain. This has been implemented as a package for the Robot Operating System (ROS) for the PR-2 robot. Their work is similar to ours, but it relies on establishing correspondences between point features in the laser scans and the camera image. To do so, they use the reflectance values of the laser scan points to locate the checkerboard corners in the laser scans. However, reflectance values can be greatly affected by scanning geometry and ambient lighting, making checkerboard detection difficult. Furthermore, the checkerboard corners are likely to lie in between laser scan points, and attempting to account for such localization errors in the laser scans will make the minimization relatively complicated. Instead, by using only the range values in the laser scans, the noise in the calibration data can be easily modelled by minimizing the ``line-of-sight'' errors, as described in §7.

3. Geometric Model

3.1. Notation

We use non-bold characters x to represent scalars, bold lower case letters $\mathbf{x}$ to represent vectors, a hat symbol $\hat{\mathbf{x}}$ to represent unit vectors, a tilde symbol $\tilde{\mathbf{x}}$ to represent homogeneous coordinates, and bold upper case letters $\boldsymbol{A}$ to represent matrices.

A coordinate frame belonging to a body $\mathcal{A}$ is denoted by $^{\mathcal{A}}\mathcal{F}$, and its constituent axes by $^{\mathcal{A}}\mathcal{X}$, $^{\mathcal{A}}\mathcal{Y}$, and $^{\mathcal{A}}\mathcal{Z}$. The coordinates of a point $\mathbf{x}$ with respect to the coordinate frame $\mathcal{A}$ is denoted by $^{\mathcal{A}}\mathbf{x}$. $^{B}_{A}\boldsymbol{H}$ denotes the homogeneous transformation matrix from $^{\mathcal{A}}\mathcal{F}$ to $^{\mathcal{B}}\mathcal{F}$, such that $^{\mathcal{A}}\tilde{\mathbf{x}} = {^{B}_{A}}\boldsymbol{H}\,{^{\mathcal{B}}}\tilde{\mathbf{x}}$.

3.2. Coordinate Frames

We attach a coordinate frame $^{\mathcal{L}}\mathcal{F}$ to the mirror center of the LRF (Fig. 1). The LRF rotates around a rotational axis (green line in Fig. 1) that is parallel to $\hat{\boldsymbol{\omega}}$ and passes through a point $\mathbf{u}$ with respect to the origin of $^{\mathcal{L}}\mathcal{F}$. We denote the rotation angle of the LRF around the rotational axis by θ, and index it by i. The LRF coordinate frame after a rotation to θ_i is denoted by $^{\mathcal{L}_i}\mathcal{F}$.

The laser beam of the LRF sweeps out the $^{\mathcal{L}}\mathcal{X}$-$^{\mathcal{L}}\mathcal{Y}$ plane. We denote the angle of the laser beam from the $^{\mathcal{L}}\mathcal{X}$-axis by ϕ and indexed it by j. When the LRF is at rotation angle θ_i, a range measurement ρ_{ij} at beam
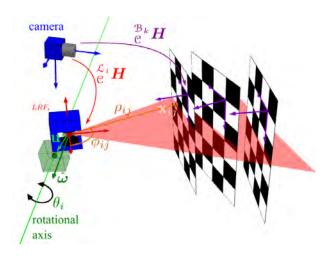

Fig. 1. *Coordinate frames and transforms used in calibration*

azimuth angle ϕ_{ij} corresponds to a point with coordinates $^{\mathcal{L}_i}\mathbf{x}_{ij} = [\rho_{ij}\cos\phi_{ij}, \rho_{ij}\sin\phi_{ij}, 0]^\top$ with respect to $^{\mathcal{L}_i}\mathcal{F}$.

We attach a coordinate frame $^{\mathcal{C}}\mathcal{F}$ to the camera center, which does not move during calibration. We index the checkerboards used in the calibration by k, and denote them as $\mathcal{B}_k$, attaching a coordinate frame $^{\mathcal{B}}\mathcal{F}$ at each of their origin. The plane of the checkerboards are denoted as $\boldsymbol{\pi}_k$, with normal $\hat{\mathbf{n}}_k$ and distance d_k with respect to the camera coordinate frame.

3.3. Rotational Transformation of Coordinate Frames

To combine the LRF range data obtained at different rotational angles θ_i, all of the points $\mathbf{x}_{ij}$ should be converted to a common coordinate frame. A simple choice is to use the first LRF coordinate frame $^{\mathcal{L}_0}\mathcal{F}$. After a rotation of $\Delta\theta = \theta_i - \theta_0$, the transformation of the LRF coordinate frame is:

$$^{\mathcal{L}_i}_{\mathcal{L}_0}\boldsymbol{H} = \begin{bmatrix} \boldsymbol{R}_{\hat{\omega}}(\Delta\theta) & (\boldsymbol{I}_3 - \boldsymbol{R}_{\hat{\omega}}(\Delta\theta))\,\mathbf{u} \\ 0 & 1 \end{bmatrix} \quad (1)$$

Alternatively, we can attach a coordinate frame $^{\mathcal{R}}\mathcal{F}$ on the rotational axis. If the $^{\mathcal{R}}\mathcal{X}$-axis is aligned with the rotational axis, two degrees of freedom remain for the transformation from $^{\mathcal{L}_0}\mathcal{F}$ to $^{\mathcal{R}}\mathcal{F}$ - a translation along the rotational axis, and a rotation about the rotational axis. In order to fix $^{\mathcal{R}}\mathcal{F}$ unambiguously, we place its origin to lie in the $^{\mathcal{L}}\mathcal{Y}$-$^{\mathcal{L}}\mathcal{Z}$ plane, and its orientation is chosen as the one having the minimal rotation from $^{\mathcal{L}_0}\mathcal{F}$, as shown in Fig. 2.

Thus, given the direction $\hat{\boldsymbol{\omega}} = [\omega_x, \omega_y, \omega_z]^\top$ and a point $\mathbf{u} = [u_x, u_y, u_z]^\top$ on the rotational axis with respect to $^{\mathcal{L}_0}\mathcal{F}$, the transformation from $^{\mathcal{R}}\mathcal{F}$ to $^{\mathcal{L}_0}\mathcal{F}$ is:

$$^{\mathcal{L}_0}_{\mathcal{R}}\boldsymbol{H} = \begin{bmatrix} \boldsymbol{R}_{\hat{a}}(\psi)^\top & -\boldsymbol{R}_{\hat{a}}(\psi)^\top \mathbf{u}^* \\ 0 & 1 \end{bmatrix} \quad (2)$$
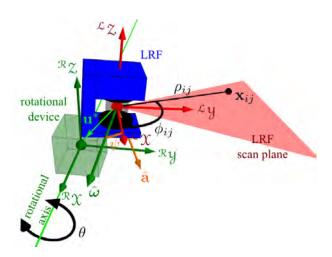
where,

Fig. 2. *Coordinate frames of the rotational device and the LRF. The axis of rotation of a rotating LRF relative to its mirror center has 4 degree of freedoms: 2 for the offset distance* $\mathbf{u}^* = [0, u_y^*, u_z^*]^\top$ *in the* $\mathcal{Y} - \mathcal{Z}$ *plane of the LRF, and 2 for the unit vector* $\hat{\boldsymbol{\omega}}$ *in the direction of the rotational axis*

$$\mathbf{u}^* = \mathbf{u} - \frac{u_x}{\omega_x}\hat{\boldsymbol{\omega}} = \begin{bmatrix} 0 \\ u_y - \frac{u_x}{\omega_x}\omega_y \\ u_z - \frac{u_x}{\omega_x}\omega_z \end{bmatrix} \qquad (3)$$

$$\hat{\mathbf{a}} = \frac{\hat{\mathbf{i}} \times \hat{\boldsymbol{\omega}}}{\|\hat{\mathbf{i}} \times \hat{\boldsymbol{\omega}}\|} = \frac{1}{\sqrt{\omega_y^2 + \omega_z^2}} \begin{bmatrix} 0 \\ -\omega_z \\ \omega_y \end{bmatrix} \qquad (4)$$

$$\psi = \cos^{-1}(\hat{\mathbf{i}} \cdot \hat{\boldsymbol{\omega}}) = \cos^{-1}(\omega_x) \qquad (5)$$

and

$$\mathbf{R}_{\hat{\mathbf{a}}}(\psi) = \begin{bmatrix} \omega_x & -\omega_y & -\omega_z \\ \omega_y & \omega_x + \omega_z^2 \frac{1-\omega_x}{\omega_y^2+\omega_z^2} & -\omega_y\omega_z\frac{1-\omega_x}{\omega_y^2+\omega_z^2} \\ \omega_z & -\omega_y\omega_z\frac{1-\omega_x}{\omega_y^2+\omega_z^2} & \omega_x + \omega_y^2\frac{1-\omega_x}{\omega_y^2+\omega_z^2} \end{bmatrix}$$
$$(6)$$

After a rotation of $\Delta\theta = \theta_i - \theta_0$, the transformation from $^\mathcal{R}\mathcal{F}$ to $^{\mathcal{L}_i}\mathcal{F}$ is thus:

$$^{\mathcal{L}_i}_{\mathcal{R}}\boldsymbol{H} = \begin{bmatrix} \boldsymbol{R}_{\hat{\boldsymbol{\omega}}}(\Delta\theta)\boldsymbol{R}_{\hat{\mathbf{a}}}(\psi)^\top & -\boldsymbol{R}_{\hat{\boldsymbol{\omega}}}(\Delta\theta)\boldsymbol{R}_{\hat{\mathbf{a}}}(\psi)^\top\mathbf{u}^* \\ 0 & 1 \end{bmatrix}$$
$$(7)$$

3.4. Representation of the Rotational Axis

In Eq. (1), the rotational axis is represented by a point $\mathbf{u}$ and a direction $\hat{\boldsymbol{\omega}}$, giving a total of 5 DOF. However, since $\mathbf{u}$ is a vector from the origin of $^\mathcal{L}\mathcal{F}$ to any point on the rotational axis, another point $\mathbf{u}' = \mathbf{u} + \lambda\hat{\boldsymbol{\omega}}$ for any $\lambda \in \mathbb{R}$ can also be used. In Eq. (2) and (7), $\mathbf{u}$ is replaced by $\mathbf{u}^* = [0, u_y^*, u_z^*]^\top$, a point constrained to $^\mathcal{L}\mathcal{Y}$-$^\mathcal{L}\mathcal{Z}$ plane, leaving it with only 2 DOF.

Another way to represent the rotational axis is to make use of the vector product $\mathbf{v} = \hat{\boldsymbol{\omega}} \times \mathbf{u}$, known as the moment of the line, which is invariant under the choice of $\mathbf{u}$, since $\mathbf{v}' = \hat{\boldsymbol{\omega}} \times (\mathbf{u} + \lambda\hat{\boldsymbol{\omega}}) = \hat{\boldsymbol{\omega}} \times \mathbf{u} = \mathbf{v}$. The

pair of vectors $(\hat{\boldsymbol{\omega}}, \mathbf{v})$ are known as the Plücker coordinates of the line [12]. The two vectors must satisfy the constraint $\hat{\boldsymbol{\omega}} \cdot \mathbf{v} = 0$, and are defined up to scale, so $(\lambda\hat{\boldsymbol{\omega}}, \lambda\mathbf{v})$ for any $\lambda \neq 0$ defines the same line; thus, there are 4 DOF within the six parameters of $\hat{\boldsymbol{\omega}}$ and $\mathbf{v}$.

Given the Plücker coordinates $(\boldsymbol{\omega}, \mathbf{v})$ of a line, we can go back to the point and direction representation by finding a point $\mathbf{u}$ on the line, which can be obtained simply as [12]:

$$\mathbf{u} = \frac{\mathbf{v} \times \boldsymbol{\omega}}{\|\boldsymbol{\omega}\|^2} \qquad (8)$$

4. Overview of Calibration Procedure

4.1. Data Acquisition

Fig. 3. *Calibration setup: 3 or more planar calibration patterns are scanned by the rotating LRF and imaged by a static camera*

In our proposed calibration procedure, the data acquisition consists of placing $n_k \geq 3$ planar checkerboard patterns $\mathcal{B}_k$ in front of the rotating LRF to be calibrated, as shown in Fig. 3. A single image of all the checkerboards is captured to determine their poses $^{\mathcal{B}_k}_{\mathcal{C}}\boldsymbol{H}$ relative to the camera coordinate frame. The LRF is rotated to $n_i \geq 2$ different angles θ_i, at each of which a scan $\mathcal{S}_i = \{\mathbf{x}_{ij}\}$ of the checkerboards are made. The set of points in each scan $\mathcal{S}_i$ belonging to checkerboard $\mathcal{B}_k$ is denoted by $\mathcal{S}_{i,k} = \{\mathbf{x}_{ij} \mid \mathbf{x}_{ij} \in \mathcal{B}_k\}$.

Instead of using n_k different checkerboards and scanning them all at once, one single checkerboard can be scanned n_k times at different poses, giving an equivalent set of scan points $\{\mathcal{S}_{i,k}\}$.

4.2. Data Processing

The objective of the calibration is to estimate the parameters of the rotational axis, $(\hat{\boldsymbol{\omega}}, \mathbf{v})$. In order to do so, we propose a calibration procedure with the three steps outlined in Algorithm 1 and illustrated in Fig. 4.

Step 1 is equivalent to performing a calibration between a camera and a static 2D-LRF. This can be accomplished using any of the existing methods mentioned in §2. However, as we will explain in §5, static camera-LRF calibration can be modelled as a kinematics point-plane constraints problem. Doing so allows us to use the minimum number of calibration boards, reducing the amount time for data acquisition and processing.

Algorithm 1 Calibration Procedure

1) Initial static camera-LRF calibration
   Using scan $\mathcal{S}_0$, determine the pose $^{\mathcal{L}_0}_{\mathcal{C}}\boldsymbol{H}$ of the LRF at the initial rotation angle θ_0 with respect to the camera.

2) Initial estimate of the rotational axis $(\hat{\boldsymbol{\omega}}, \mathbf{v})$

   a) Estimate the final LRF pose $^{\mathcal{L}_{n_i}}_{\mathcal{C}}\boldsymbol{H}$
      Using scan $\mathcal{S}_{n_i}$, determine the pose of the LRF at the final rotation angle θ_{n_i}.

   b) Extract $(\hat{\boldsymbol{\omega}}, \mathbf{v})$ from $^{\mathcal{L}_{n_i}}_{\mathcal{L}_0}\boldsymbol{H}$ using the screw decomposition

3) Nonlinear refinement of $^{\mathcal{L}_0}_{\mathcal{C}}\boldsymbol{H}$ and $(\hat{\boldsymbol{\omega}}, \mathbf{v})$.
   Given $^{\mathcal{L}_0}_{\mathcal{C}}\boldsymbol{H}$ and $(\hat{\boldsymbol{\omega}}, \mathbf{v})$, the expected scan data $\{\mathcal{S}^+_{i,k}\}$ can be calculated. The task then is to find the optimal $^{\mathcal{L}_0}_{\mathcal{C}}\boldsymbol{H}^+$ and $(\hat{\boldsymbol{\omega}}^+, \mathbf{v}^+)$ which minimizes the differences between $\{\mathcal{S}_{i,k}\}$ and $\{\mathcal{S}^+_{i,k}\}$

Step 2 is used to obtain an initial estimate for the parameters of the rotational axis $(\hat{\boldsymbol{\omega}}, \mathbf{v})$. First, the static calibration of step 1 is repeated, but with the LRF at the final rotational angle θ_{n_i}. The rotational axis can then be extracted using the screw decomposition, as we will explain in §6. An initial estimate for $(\hat{\boldsymbol{\omega}}, \mathbf{v})$ can also be obtained through other means, such as using manual measurement or mechanical drawings. In such cases, step 2 can be skipped.

In step 3, starting with initial value for $^{\mathcal{L}_0}_{\mathcal{C}}\boldsymbol{H}$ and $(\hat{\boldsymbol{\omega}}, \mathbf{v})$, we use nonlinear optimization to find the optimal estimates $^{\mathcal{L}_0}_{\mathcal{C}}\boldsymbol{H}^+$ and $(\hat{\boldsymbol{\omega}}^+, \mathbf{v}^+)$ which minimizes the errors between the actual scan data $\{\mathcal{S}_{i,k}\}$ and the expected scan values $\{\mathcal{S}^+_{i,k}\}$, which we will describe in detail in §7.

5. Step 1: Static Camera-LRF Calibration using Point-Plane Constraints
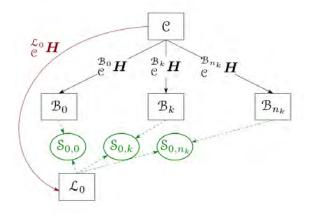
5.1. Kinematics Point-Plane Constraints

In the point-plane constraints problem, n points $\mathbf{x}_i$ on a rigid body $\mathcal{B}$ are constrained to lie on n planes $\boldsymbol{\pi}_i$ whose parameters are known with respect to a ground coordinate frame $^{\mathcal{G}}\mathcal{F}$ (Fig. 5). The goal is to recover all possible poses $^{\mathcal{B}}_{\mathcal{G}}\boldsymbol{H}$ of the body $\mathcal{B}$ with respect to $^{\mathcal{G}}\mathcal{F}$.
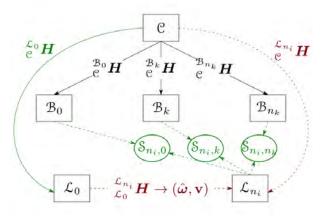
This is a problem studied in kinematics. In [13], Selig shows, using algebraic geometry, that with a minimum of 6 point-plane constraints, up to 8 solutions can be obtained. In [14, 15], Wampler shows equivalent results, along with numerical methods for obtaining the solutions.
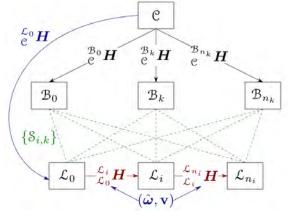
5.2. Modelling Static Camera-LRF Calibration

Treating the LRF as the body $\mathcal{B}$ and the camera coordinate frame as the ground coordinate frame $^{\mathcal{G}}\mathcal{F}$, it is straightforward to see that the static camera-LRF calibration problem can be modelled as a point-plane constraints problem. The LRF is able to measure points $\mathbf{x}_{ij}$ with respect to its own coordinate frame $^{\mathcal{L}}\mathcal{F}$. These points are known to lie on a checkerboard plane $\boldsymbol{\pi}_k$ imaged by the camera. Thus, the plane parameters

(a) Step 1: Initial static calibration

(b) Step 2: Initial estimate of the rotational axis $(\hat{\boldsymbol{\omega}}, \mathbf{v})$

(c) Step 3: Refinement of $^{\mathcal{L}_0}_{C}\boldsymbol{H}$ and $(\hat{\boldsymbol{\omega}}, \mathbf{v})$

Fig. 4. Calibration Procedure

$(\hat{\mathbf{n}}_k, d_k)$ are known with respect to the camera coordinate frame $^{\mathcal{C}}\mathcal{F}$. Each checkerboard pattern scanned by the LRF and imaged by the camera gives one line-on-plane constraint, which is equivalent to two independent point-on-plane constraints, as any other point on the same line will give a redundant point-on-plane constraint. With 3 checkerboards, we obtain the minimum number of $n = 6$ to solve the point-plane constraints problem.

5.3. Numerical Solution

For a point $\mathbf{x}_{ij}$ in the body coordinate frame $^{\mathcal{B}}\mathcal{F}$, it lies on a plane $\boldsymbol{\pi}_k$ with normal $\hat{\mathbf{n}}_k$ at a distance d_k from

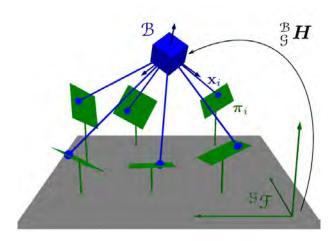**Fig. 5.** *The kinematics point-plane constraints problem*

the origin in $^{\mathcal{G}}\mathcal{F}$ if:

$$\hat{\mathbf{n}}_k^\top \left(\boldsymbol{R}\, \mathbf{x}_{ij} + \mathbf{t} \right) + d_k = 0 \qquad (9)$$

Here, $\boldsymbol{R} \in SO(3)$ and $\mathbf{t} \in \mathbb{R}^3$ are the rotation and translation of the transformation $^{\mathcal{B}}_{\mathcal{G}}\boldsymbol{H}$ from $^{\mathcal{G}}\mathcal{F}$ to $^{\mathcal{B}}\mathcal{F}$.

Using a quaternion $\boldsymbol{q} = [q_w, q_x, q_y, q_z]^\top$ to represent a rotation as $\boldsymbol{R} = \frac{1}{\boldsymbol{q}^\top \boldsymbol{q}}\boldsymbol{R}(\boldsymbol{q})$, (9) can be rewritten as:

$$\begin{aligned} F_{ijk}(\mathbf{q}, \mathbf{t}) &= \hat{\mathbf{n}}_k^\top \left(\boldsymbol{R}(\mathbf{q})\, \mathbf{x}_{ij} \right) + \mathbf{q}^\top \mathbf{q}\, d_k + \mathbf{q}^\top \mathbf{q}\, \hat{\mathbf{n}}_k^\top \mathbf{t} = 0 \\ &= \mathbf{q}^\top \boldsymbol{M}_{ijk} \mathbf{q} + \mathbf{q}^\top \mathbf{q}\, \hat{\mathbf{n}}_k^\top \mathbf{t} \end{aligned}$$
$$(10)$$

Here, the quaternion $\mathbf{q}$ is a homogeneous vector in $\mathbb{P}^3$, and not necessarily a unit vector as is commonly employed. This was done to avoid the need to impose a quadratic constraint. As a result, the scalar product $\mathbf{q}^\top \mathbf{q}$ appears in the denominator to normalize the quaternion. $\boldsymbol{M}_{ijk}$ is a 4×4 symmetric matrix containing the elements of $\mathbf{x}_{ij}$, $\hat{\mathbf{n}}_k$, and d_k.

Given n point-plane constraints, a system of n equations in the form of Eq. (10) is obtained, which is quadratic in $\mathbf{q}$ and linear in $\mathbf{t}$. The linear terms $\mathbf{q}^\top \mathbf{q}\, \mathbf{t}$ can be eliminated through Gaussian elimination, leaving $n - 3$ equations in $\mathbf{q}$. For the minimum case of $n = 6$, we obtain a system of 3 quadratic polynomials in the 3 free variables of $\mathbf{q}$, which gives up to 8 solutions. This can be solved using Gröbner bases [16]. In [14, 15], Wampler gives a eigenvalue-based numerical solution, which he calls ``*numerical Gröbner bases*''.

For $n > 6$, we can find a unique solution by solving subsets of the n constraints and find the common solution among them. However, if there is noise in the data, there will be no solution that can simultaneously satisfy all the constraint equations. Instead, Wampler gives linear solutions for the separate cases of $n = 7$, $8 \geq n > 12$, and $n \geq 12$. In the following, we give a brief review of the solution for $8 \geq n > 12$. The reader is referred to Wampler's papers [14, 15] for further details.

Eq. (10) can be rewritten in a linear form in terms of the 2nd degree monomials of $\mathbf{q}$:

$$F_{ijk}(\mathbf{q}, \mathbf{t}) = \boldsymbol{C}_{ijk}\tilde{\mathbf{q}} + \mathbf{q}^\top \mathbf{q}\, \hat{\mathbf{n}}_k^\top \mathbf{t} \qquad (11)$$

Here, $\boldsymbol{C}_{ijk}$ is a 1×10 vector with rearranged entries of $\boldsymbol{M}_{ijk}$, and $\tilde{\mathbf{q}}$ is a 10×1 vector with the 2nd degree monomials of $\mathbf{q}$ in lexicographical ordering: $\tilde{\mathbf{q}} = [q_w{}^2, q_w q_x, q_w q_y, q_w q_z, q_x{}^2, q_x q_y, q_x q_z, q_y{}^2, q_y q_z, q_z{}^2]^\top$.

With n points on n planes, we can stack the constraints of Eq. (11) to get a system of equations:

$$F(\mathbf{q}, \mathbf{t}) = \boldsymbol{C}\tilde{\mathbf{q}} + \mathbf{q}^\top \mathbf{q}\, \boldsymbol{N}\mathbf{t} \qquad (12)$$

Here, $\boldsymbol{C}$ is a $n \times 10$ matrix, and $\boldsymbol{N}$ is a $n \times 3$ matrix containing the normal vectors $\hat{\mathbf{n}}_k^\top$. To solve this system, we need to have $rank(\boldsymbol{N}) = 3$, meaning that the normal vectors of the planes should span 3-space.

Pre-multiplying Eq. (12) with $\boldsymbol{N}^\perp$, a $(n-3) \times n$ matrix spanning the left null space of $\boldsymbol{N}$, we reduce the system to a set of $n - 3$ homogeneous quadratic polynomials in $\mathbf{q}$:

$$F(\mathbf{q}) = \boldsymbol{N}^\perp \boldsymbol{C}\tilde{\mathbf{q}} \qquad (13)$$

This can be minimized using SVD, with the solution $\tilde{q}$ being the right singular vector corresponding to the smallest singular value. The rotation $\boldsymbol{R}(\boldsymbol{q})$ is extracted from $\tilde{q}$ and substituted back in (12) to recover the translation $\mathbf{t}$.

5.4. Minimal Conditions

In the camera-LRF calibration method given by Zhang [1], a linear solution is given to obtain an initial estimate for the camera to LRF transformation $^{\mathcal{L}}_{\mathcal{C}}\boldsymbol{H}$. Each line-on-plane correspondence gives two independent equations in nine unknown parameters, so a minimum of 5 LRF scan and image pairs are needed.

In Wasielewski's calibration method [3] using LRF point on image line correspondences, each set of correspondence gives one constraint equation in nine unknown parameters, so a minimum of 9 LRF scan and image pairs are needed. In Li's method [4] which uses a calibration target giving two image lines, a minimum of 5 LRF scan and image pairs are needed.

As mentioned above, a line-on-plane correspondence can be modelled as two point-plane constraints. As we describe in [17], a point-on-image-line correspondence can also be modelled as a point-plane constraint, where the plane passes through the camera center and the image line. Table 1 shows a summary of the minimum number of LRF-scan and image pairs required by the different methods, as well as the minimum conditions when modelled using point-plane constraints.

Although usually, it is preferable to use more laser scans and image pairs to provide redundant data to reduce the effects of noise, leading to more accurate calibration results. However, we use the fact that we already have a lot of redundant data from the scans $\{\mathcal{S}_i\}$ at different rotational angles θ_i. Thus, we are motivated to find the minimal solution for the initial static

Tab. 1. *Minimum LRF-scan and image pairs*

Method	Correspondences	Scan-Image Pairs	
		Original	Point-Plane
Zhang [1]	line-on-plane	5	3 (4)*
Wasielewski [3]	point-on-image-line	9	6 (7)*
Li [4]	point-on-image-line	5	3 (4)*

*number in brackets indicate pairs required for unique solution

camera-LRF calibration step, and instead rely on using redundant data over all the rotational angles θ_i in the final minimization described in §7 to reduce the effects of noise in the calibration.

Although using point-plane constraints to model the different type of correspondences reduces the minimal scan-image pairs required only very slightly, the advantage of using point-plane constraints is that all types of correspondences can be modelled uniformly and solved using a single method.

6. Step 2: Initial Estimate of the Rotational Axis using Screw Decomposition

Using the static camera-LRF calibration method described in §5, we obtain an initial estimate for ${}^{\mathcal{L}_0}_{\mathcal{C}}\boldsymbol{H}$ and ${}^{\mathcal{L}_{n_i}}_{\mathcal{C}}\boldsymbol{H}$ for step 1 and step 2(a) respectively. Composing the camera to LRF transforms, we obtain the relative LRF motion between the two rotational angles θ_0 and θ_{n_i}:

$$
{}^{\mathcal{L}_{n_i}}_{\mathcal{L}_0}\boldsymbol{H} = \left({}^{\mathcal{L}_0}_{\mathcal{C}}\boldsymbol{H}\right)^{-1} \cdot {}^{\mathcal{L}_{n_i}}_{\mathcal{C}}\boldsymbol{H} \tag{14}
$$

According to Chasles's theorem, every spatial transformation can be decomposed as a screw displacement - a rotation about a line together with a translation along the same line [12]:

$$
{}^{\mathcal{L}_{n_i}}_{\mathcal{L}_0}\boldsymbol{H} = \begin{bmatrix} \boldsymbol{R}_{\hat{\omega}}(\Delta\theta) & {}^{\mathcal{L}_{n_i}}_{\mathcal{L}_0}\mathbf{t} \\ 0 & 1 \end{bmatrix} \tag{15}
$$

$$
= \begin{bmatrix} \boldsymbol{R}_{\hat{\omega}}(\Delta\theta) & \frac{\Delta\theta}{2\pi}p\hat{\omega} + (\boldsymbol{I}_3 - \boldsymbol{R}_{\hat{\omega}}(\Delta\theta))\mathbf{u} \\ 0 & 1 \end{bmatrix} \tag{16}
$$

Eq. (16) is known as the "*screw matrix*" [12, 18], representing a rotation of angle $\Delta\theta$ around a line called the screw axis that has direction $\hat{\omega}$ and passes through the point $\mathbf{u}$. p is the pitch of the screw motion, corresponding to the translation along $\hat{\omega}$ for every revolution around the screw axis. Compared with Eq. (15), while the rotation matrix remains the same, the translation has been decomposed into a translation along the rotational axis $\frac{\Delta\theta}{2\pi}p\hat{\omega}$, and a translation perpendicular to the rotational axis $(\boldsymbol{I}_3 - \boldsymbol{R}_{\hat{\omega}}(\Delta\theta))\mathbf{u}$.

Given $\boldsymbol{R}_{\hat{\omega}}(\Delta\theta)$ and ${}^{\mathcal{L}_{n_i}}_{\mathcal{L}_0}\mathbf{t}$ of the relative LRF motion from θ_0 and θ_{n_i}, we can recover the parameters of its equivalent screw displacement as:

$$
p = \frac{2\pi}{\Delta\theta}\hat{\omega} \cdot {}^{\mathcal{L}_{n_i}}_{\mathcal{L}_0}\mathbf{t} \tag{17}
$$

$$
\mathbf{u} = (\boldsymbol{I}_3 - \boldsymbol{R}_{\hat{\omega}}(\Delta\theta))^{\dagger}\left({}^{\mathcal{L}_{n_i}}_{\mathcal{L}_0}\mathbf{t} - \frac{\Delta\theta}{2\pi}p\hat{\omega}\right) \tag{18}
$$

Since $(\boldsymbol{I}_3 - \boldsymbol{R}_{\hat{\omega}}(\Delta\theta))\hat{\omega} = \boldsymbol{0}$, $(\boldsymbol{I}_3 - \boldsymbol{R}_{\hat{\omega}}(\Delta\theta))$ is a singular matrix; thus, its pseudo-inverse is used in Eq. (18) to recover $\mathbf{u}$.

Ideally, the decomposition of the relative motion ${}^{\mathcal{L}_{n_i}}_{\mathcal{L}_0}\boldsymbol{H}$ of the LRF from angle θ_0 to θ_{n_i} will give a screw displacement with zero pitch $p = 0$, and the screw axis $(\hat{\omega}, \mathbf{v})$ is the rotational axis of the LRF. Furthermore, if we repeat the static camera-LRF calibration at another rotation angle θ_i and compute ${}^{\mathcal{L}_i}_{\mathcal{L}_0}\boldsymbol{H}$, the screw decomposition should give the same screw axis $(\hat{\omega}, \mathbf{v})$. However, with noise in the calibration data, such ideal results will not be obtained. The task then remains to finding the optimal rotational axis $(\hat{\omega}^+, \mathbf{v}^+)$ that minimizes some error function which accounts for the noise in the calibration data.

7. Step 3: Nonlinear Refinement

The linear solution to the point-plane constraints problem given in §5.3 minimizes an algebraic error. To find the optimal calibration parameters, an optimization that minimizes a meaningful geometric error should be performed. The error function most commonly used in static camera-LRF calibration is the point-to-plane distance e_{jk}^{PP}:

$$
\arg\min_{{}^{\mathcal{L}}_{\mathcal{C}}\boldsymbol{H}} \sum_{j,k} e_{jk}^{PP^2} = \sum_{j,k} \left\| \mathbf{n}_k^\top (\boldsymbol{R}\,\mathbf{x}_j + \mathbf{t}) + d_k \right\|^2 \tag{19}
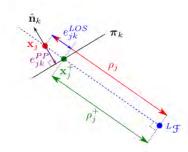$$

Fig. 6. *Point-to-plane error e_{jk}^{PP} vs. line-of-sight error e_{jk}^{LOS}*

As shown in Fig. 6, this is the perpendicular distance from the plane $\boldsymbol{\pi}_k$ to the point $\mathbf{x}_j$. However, if we assume that the points $\mathbf{x}_j = f(\phi_j, \rho_j)$ measured by the LRF contains only zero-mean Gaussian noise ${}^{\mathcal{L}}w_j \sim N(0, {}^{\mathcal{L}}\sigma^2)$ in its range values ρ_j, so $\rho_j = \rho_j^+ + {}^{\mathcal{L}}w_j$, then instead of the point-to-plane errors e_{jk}^{PP}, a better error to minimize is the "*line-of-sight*" distance e_{jk}^{LOS}, as illustrated in Fig. 6.

$$\arg\min_{^{\mathcal{L}}_{\mathcal{C}} \boldsymbol{H}} \sum_{j,k} e_{jk}^{LOS^2} = \sum_{j,k} \|\mathbf{x}_j^+ - \mathbf{x}_j\|^2$$
$$= \sum_{j,k} \|\rho_j^+ - \rho_j\|^2 \qquad (20)$$

In Eq. (20), given plane $\boldsymbol{\pi}_k : (\hat{\mathbf{n}}_k, d_k)$ for the kth plane, the ideal coordinates $\mathbf{x}_j^+$ is calculated as the intersection point of the plane $\boldsymbol{\pi}_k$ with the line passing through the LRF mirror center and the measured point $\mathbf{x}_j$. Using $\hat{\mathbf{x}}_j$ to denote $\frac{\mathbf{x}_j}{\|\mathbf{x}_j\|}$:

$$\mathbf{x}_j^+ = \frac{-d_k - \mathbf{t}^\top \mathbf{n}_k}{\hat{\mathbf{x}}_j^\top \boldsymbol{R}^\top \mathbf{n}_k} \hat{\mathbf{x}}_j \qquad (21)$$

Ignoring errors in $\boldsymbol{\pi}_k : (\hat{\mathbf{n}}_k, d_k)$, Eq. (20) gives a maximum likelihood estimate for $\boldsymbol{R}, \mathbf{t}$. To account for errors in the pose of the checkerboard planes $\boldsymbol{\pi}_k : (\hat{\mathbf{n}}_k, d_k)$ estimated by the camera, assuming zero-mean Gaussian noise $^{\mathcal{C}}w_j \sim N(0, ^{\mathcal{C}}\sigma^2)$ in the image coordinates $\mathbf{y}_j$ of the checkerboard corners with 3D coordinates $\mathbf{b}_j$, the minimization can be augmented with the image reprojection errors of the checkerboard corners:

$$\arg\min_{^{\mathcal{L}}_{\mathcal{C}} \boldsymbol{H}, ^{\mathcal{B}_k}_{\mathcal{C}} \boldsymbol{H}} \frac{^{\mathcal{C}}\sigma^2}{n_\mathbf{x}{}^{\mathcal{L}}\sigma^2 + n_\mathbf{y}{}^{\mathcal{C}}\sigma^2} \sum_{j,k} \|\mathbf{x}_j^+ - \mathbf{x}_j\|^2 +$$
$$\frac{^{\mathcal{L}}\sigma^2}{n_\mathbf{x}{}^{\mathcal{L}}\sigma^2 + n_\mathbf{y}{}^{\mathcal{C}}\sigma^2} \sum_{j,k} \|\mathbf{y}_j - \boldsymbol{K} \cdot \left(^{\mathcal{B}_k}_{\mathcal{C}} \boldsymbol{R} \mathbf{b}_j + ^{\mathcal{B}_k}_{\mathcal{C}}\mathbf{t}\right)\|^2 \qquad (22)$$

Here, $^{\mathcal{B}_k}_{\mathcal{C}} \boldsymbol{H} = \begin{bmatrix} ^{\mathcal{B}_k}_{\mathcal{C}} \boldsymbol{R} & ^{\mathcal{B}_k}_{\mathcal{C}}\mathbf{t} \\ 0 & 1 \end{bmatrix}$ is the pose of the kth checkerboard with respect to the camera. $n_\mathbf{x}$ is the number of laser scan points $\mathbf{x}_j$, and $n_\mathbf{y}$ is the number of checkerboard corners $\mathbf{y}_j$.

To estimate the optimal parameters $(\hat{\boldsymbol{\omega}}^+, \mathbf{v}^+)$ for the LRF rotational axis, we perform the minimization with all points $\mathbf{x}_{ij}$ obtained over all rotational angles $\theta_i, i = 0, \ldots, n_i$:

$$\arg\min_{^{\mathcal{L}_0}_{\mathcal{C}} \boldsymbol{H}, \hat{\boldsymbol{\omega}}, \mathbf{v}, ^{\mathcal{B}_k}_{\mathcal{C}} \boldsymbol{H}} \frac{^{\mathcal{C}}\sigma^2}{n_\mathbf{x}{}^{\mathcal{L}}\sigma^2 + n_\mathbf{y}{}^{\mathcal{C}}\sigma^2} \sum_{i,j,k} \|\mathbf{x}_{ij}^+ - \mathbf{x}_{ij}\|^2 +$$
$$\frac{^{\mathcal{L}}\sigma^2}{n_\mathbf{x}{}^{\mathcal{L}}\sigma^2 + n_\mathbf{y}{}^{\mathcal{C}}\sigma^2} \sum_{j,k} \|\mathbf{y}_j - \boldsymbol{K} \cdot \left(^{\mathcal{B}_k}_{\mathcal{C}} \boldsymbol{R} \mathbf{b}_j + ^{\mathcal{B}_k}_{\mathcal{C}}\mathbf{t}\right)\|^2 \qquad (23)$$

In this optimization, only the pose of the LRF at the first rotational angle $^{\mathcal{L}_0}_{\mathcal{C}} \boldsymbol{H}$ is directly included as parameters; the pose of the LRF at the other rotational angles $^{\mathcal{L}_i}_{\mathcal{C}} \boldsymbol{H}$ are calculated from $(\hat{\boldsymbol{\omega}}, \mathbf{v})$ using Eq. (1) and (8).

8. Experimental Results

To test our calibration algorithm, we use the LRF (SICK LMS-100) mounted on a pan-tilt unit (Directed Perception PTU-D46), as shown in Fig. 7.
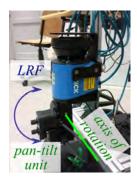

Fig. 7. *The 2D LRF mounted on a pan-tilt unit used in our calibration*

Fig. 8 shows the checkerboards setup for our calibration, with the checkerboard patterns being automatically detected using OpenCV. Instead of using the minimum of 3 planes, which would give up to 8 solutions for the initial static camera-LRF calibration, 4 planes are used to simplify the computation. As described in §5, the normals $\{\hat{\mathbf{n}}_k\}$ of the checkerboard planes $\{\boldsymbol{\pi}_k\}$ should span $\mathbb{R}^3$, so care must be taken so that not all of the checkerboards are vertical. For example, if only the vertical walls in a room are used, $\{\hat{\mathbf{n}}_k\}$ would only span $\mathbb{R}^2$, giving a degenerate configuration.

Fig. 8. *Checkerboard patterns extracted in camera image*

Fig. 9 shows a single laser scan, with points belonging to the checkerboards identified by running RANSAC line-fitting over the scan data multiple times.
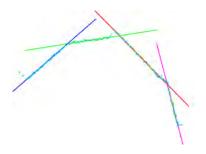

Fig. 9. *Points in each laser scan belonging to the checkerboards are extracted using RANSAC line-fitting*

For the final optimization in Eq.(23), we used $^{\mathcal{L}}\sigma = 12\text{mm}$, corresponding to the statistical error of the LMS-100 as given by the manufacturer, and $^{\mathcal{C}}\sigma = 0.5\text{px}$ for the image localization noise. The results of our calibration are tabulated in Table 2, and

checkerboards reconstructed using these parameters are shown in Fig. 10. The reconstruction of a small indoor environment after calibration is shown in Fig. 11.

Tab. 2. *Calibration Results*

Parameter	Initial	Final
Axis Translation Offset (mm)	$[0, -30, 160]$	$[0, -27.6, 158.9]$
Axis Rotational Offset	$0°$	$10.14°$
Line-of-Sight Error (mm)	8.08	7.24

Fig. 10. *Laser points with intensity values reconstructed after calibration, showing a rough outline of the scanned checkerboard patterns*
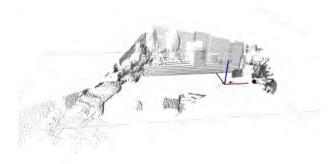

Fig. 11. *Indoor environment reconstructed after calibration*

The calibration results show a small change in the location and orientation of the rotation axis, as well as a slight decrease in the line-of-sight errors. Although the final parameters of the rotational axis differ only slightly from those obtained using hand measurement, it accounts for all the degrees of freedom of the rotational axis. Furthermore, although the reconstructed checkerboards show only modest improvements, the importance of proper calibration will be more noticeable for data with larger range, as well as when fusing the range data with image data.

9. Conclusions

In this paper, we proposed a method for recovering the rotational axis of a rotating 2D LRF. Instead of assuming that the rotational axis is aligned with one of the primary axis of the LRF, we model it as a line in 3D space with 4 DOF. The calibration consists of performing static camera-LRF calibration at two different rotational angle to obtain an initial estimate, followed by a nonlinear optimization to refine the results.

However, instead of using existing static camera-LRF calibration methods, we model it as a kinematics point-plane constraints problem. This allows us to minimize the number of calibration planes that are needed, simplifying the calibration; also, various types of correspondences can be handled in a uniform manner. Furthermore, we describe the minimization of the ``line-of-sight'' errors, which directly models the noise in the range measurements of a LRF.

AUTHORS

Edmond Wai Yan So* - IAS Lab, UNIPD, Padua, Italy, e-mail: edmond.so@dei.unipd.it.

Filippo Basso - IAS, e-mail: filippo.basso@dei.unipd.it.

Emanuele Menegatti - IAS, e-mail: emg@dei.unipd.it.

*Corresponding author

REFERENCES

[1] Q. Zhang, R. Pless, „Extrinsic calibration of a camera and laser range finder (Improves camera calibration)", In: *IEEE/RSJ International Conference on Intelligent Robots and Systems*, vol. 3, 2004, pp. 2301-2306.

[2] C. Mei, P. Rives, „Calibration between a central catadioptric camera and a laser range finder for robotic applications", In: *IEEE International Conference on Robotics and Automation*, 2006, pp. 532-537.

[3] S. Wasielewski, O. Strauss, „Calibration of a multi-sensor system laser Rangefinder/Camera", In: *Intelligent Vehicles Symposium*, 1995, pp. 472-477.

[4] G. Li, Y. Liu, L. Dong, X. Cai, D. Zhou, „An algorithm for extrinsic parameters calibration of a camera and a laser range finder using line features", In: *IEEE/RSJ International Conference on Intelligent Robots and Systems*, 2007, pp. 3854-3859.

[5] R. Unnikrishnan, M. Hebert, „Fast extrinsic calibration of a laser rangefinder to a camera", *Tech. Rep.*, 2005.

[6] H. Surmann, K. Lingemann, A. Nüchter, J. Hertzberg, „A 3D laser range finder for autonomous mobile robots", In: *International Symposium on Robotics*, 2001.

[7] H. Surmann, A. Nüchter, J. Hertzberg, „An autonomous mobile robot with a 3D laser range finder for 3D exploration and digitalization of indoor environments", *Robotics and Autonomous Systems*, vol. 45, no. 3-4, pp. 181-198, 2003.

[8] H. Andreasson, „Local visual feature based localisation and mapping by mobile robots", Ph.D. dissertation, Örebro University, 2008.

[9] D. Scaramuzza, A. Harati, R. Siegwart, „Extrinsic self calibration of a camera and a 3D laser range finder from natural scenes", In: *IEEE/RSJ International Conference on Intelligent Robots and Systems*, 2007, pp. 4164-4169.

[10] J. Weingarten, „Feature-based 3D SLAM", Ph.D. dissertation, École Polytechnique Fédérale de Lausanne, 2006.

[11] V. Pradeep, K. Konolige, E. Berger, „Calibrating a multi-arm multi-sensor robot: A bundle adjustment approach", In: *International Symposium on Experimental Robotics*, 2010.

[12] J. M. Selig, *Geometric Fundamentals of Robotics*, 2nd ed., Springer, 2004.

[13] J. M. Selig, „On the geometry of point-plane constraints on rigid-body displacements", *Acta Applicandae Mathematicae*, 2011.

[14] C. W. Wampler, „Locating N points of a rigid body on N given planes", In: 28th *Biennial Mechanisms and Robotics Conference*, 2004, pp. 513-521.

[15] C. W. Wampler, „On a rigid body subject to point-plane constraints", *Journal of Mechanical Design*, vol. 128, no. 1, pp. 151-158, 2006.

[16] D. Cox, J. Little, D. O'Shea, *Ideals, Varieties, and Algorithms: An Introduction to Computational Algebraic Geometry and Commutative Algebra*, 2nd ed., Springer, February 2006.

[17] E. W. Y. So, E. Menegatti, „A unified approach to extrinsic calibration between a camera and a laser range finder using point-plane constraints", In: 1st *Workshop on Perception for Mobile Robots Autonomy*, 2012.

[18] J. M. McCarthy, *Geometric Design of Linkages*, 1st ed., Springer, April 2000.